AIAA Science and Technology Forum and Exposition, 6-10 January 2020, Orlando, Florida

An Investigation of Dominant Flow Features in Rotating Turbulent Pipe Flows

Jefferson Davis¹ * Sparsh Ganju¹ † Anirudh Venkatesh² † Sean Bailey¹ § and Christoph Brehm¹¶

¹Department of Mechanical Engineering, University of Kentucky, Lexington, KY 40506, USA.

²Institute of Chemical Technology, Mumbai, India.

Rotating and swirling turbulence comprises an important class of turbulent flows, not only due to the complex physics that occur, but also due to their relevance to many engineering applications, such as combustion, cyclone separation, mixing, etc. In these types of flows, rotation strongly affects the characteristics and structure of turbulence. The underlying turbulent flow phenomena are complex and currently not well understood. The axially rotating pipe flow is a well-suited prototypical case for studying rotation effects in turbulence due to its simple geometry and the ability to be reproduced experimentally in a controlled environment. By examining the complex interaction of turbulent structures within rotating turbulent pipe flow, insight can be gained into the behavior of rotating flows relevant to engineering applications.

Direct numerical simulations are conducted at a bulk Reynolds number of $Re_D = 19,000$ with rotation numbers ranging from N=0 to 3. In addition to providing turbulence statistics, proper orthogonal decomposition is used to identify the relevant (highest energy) modes of the flow and obtain an understanding about the coherence in the flow.

I. Introduction

Rotating and swirling turbulent flows are relevant to a wide range of engineering applications as part of aerospace, industrial, and natural systems. Despite the prevalence of these flows, little is known about the physical mechanisms governing the flow physics of rotational turbulence. The current research is based on Direct Numerical Simulation (DNS)¹⁻³ of axially rotating pipe flows (see Fig. 1) conducted in conjunction with experimental research currently in development at the University of Kentucky.⁴ Axially rotating pipe flows provide an excellent prototypical case for examination of turbulence suppression, as these flows eliminate unnecessary complications introduced by complex geometry and can be realized effectively in both simulation and laboratory experiment. An interesting phenomenon which can occur when rotating a turbulent flow is turbulence suppression, which has been shown to cause reduction in skin friction,⁵⁻⁹ making the understanding of turbulence suppression highly valuable for engineering applications. Turbulence suppression has been observed in notable experiments dating back to the 1960s¹⁰ and some DNS studies of rotational pipe flows have been conducted at only relatively low Reynolds numbers.^{9,11-13}

In previous efforts to examine the effects of rotation on turbulent pipe flows, Kikuyama et al.⁶ analyzed velocity distributions as well as hydraulic loss in flows with Reynolds numbers up to Re = 50,000, where $Re = U_b D/\nu$, U_b is the bulk velocity, D is the pipe diameter, and ν is the kinematic viscosity of the fluid, in a domain of L = 160D, where L is the domain length. These experiments showed a development length, L_D , of $L_D \leq 120D$ for all flows examined and confirmed the relationship between Richardson number and mixing length given by Bradshaw. Experiments by Nishibori et al.⁷ examining the inlet region of axially rotating pipe flows found that a rotating laminar region surrounds a rotating non-rotating turbulent core within the

^{*}PhD. Candidate

[†]PhD. Candidate

[‡]Undergraduate Researcher

[§]Associate Professor, AIAA member.

[¶]Assistant Professor, AIAA member.

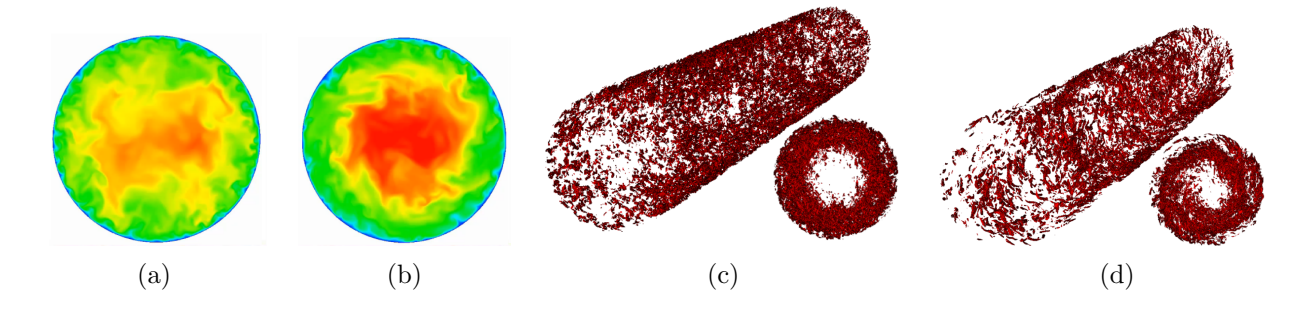


Figure 1. Comparison of (a & b) instantaneous streamwise velocity and (c & d) the corresponding Q-criterion for non-rotation (N=0) and rotating (N=1) turbulent pipe flows.

inlet region of the flow (20D < L < 60). This laminar region destabilizes downstream as the core begins to rotate, and turbulence becomes entrained in the near-wall region. Due to existence of a non-rotational turbulent region and a rotational turbulent region within the flow, it may be appropriate to describe the flow as a combination of two flow regimes 1) a turbulent pipe flow with an additional axial rotation, defined by $Re = U_b D/\nu$ or 2) a rotating flow inside a cylinder (solid body rotation) with an additional cross flow, defined by $Re_w = U_w D/2\nu$, where U_w is the velocity of the wall. Further experimental studies by Reich and Beer⁸ established a broad connection between turbulence suppression and the centrifugal force in flows $Re = 5{,}000$ to $50{,}000$ with rotation rates up to N = 5, where $N = \Omega D/2U_b$, where Ω is the angular velocity of the pipe - or equivalently, $N = Re_w/Re$.

A large number of experimental studies have been conducted to analyze the effects of rotation on turbulent pipe flows. However, numerical simulations, especially DNS, of these flows have been very limited in number (in particular at relatively higher Reynolds numbers). Feiz et al.⁹ conducted DNS of non-rotating and axially rotating pipe flows for Re = 4,900 and 7,400, and LES for axially rotating flows at Re = 20,000. An increase in N led to a reduction in skin friction and this reduction was found to be more significant at higher Reynolds numbers. Additionally, larger Re caused a decrease in the centerline velocity for the streamwise component at a given N. Orlandi & Fatica¹¹ and Orlandi & Ebstein¹² analyzed flows with rotation numbers going as high as N = 10 and up to Re = 4,900. The reduction in drag was attributed to the widening of streaks and the changing vortical structure in the near-wall region. These observations indicate that a thorough understanding of turbulence suppression can be achieved by understanding the structures in the near-wall region of rotating flows. DNS are capable of extracting data in this near-wall region which is a rather difficult task for experimental studies, necessitating the requirement of more high Reynolds number DNS.

Previously, Davis et al.^{1–3} and Brehm et al.¹⁵ have analyzed DNS of rotating pipe flow to determine the characteristics of turbulence suppression in these flows. The mean flow characteristics, Reynolds stresses, the turbulent kinetic energy (TKE) and the various terms of the TKE budget equation were analyzed. These simulations were conducted at three different Reynolds numbers — 5,300, 11,700, and 19,000 for rotation numbers, N, in the range 0-3. Additionally, this data has been used to inform RANS modeling of rotating pipe flows by Ashton et al.¹⁶ The next step in the analysis of these flows is to study the turbulent flow characteristics in more detail, in particular, the presence of coherent structures in turbulent flows. To achieve this, Proper Orthogonal Decomposition (POD) of the fluctuating velocity field is carried out.

Proper Orthogonal Decomposition (POD) is used as a tool to generate a lower-dimensional description of the structure of turbulence by producing modes arranged in order of their contribution to the total TKE by using an ensemble of signals obtained from different points in the domain. Mathematically, POD decouples the spatial and temporal aspects of turbulent structures. The eigenfunctions of the cross-correlation tensor constitute the spatial POD modes while the corresponding eigenvalues provide a description of the energy content of the corresponding mode. To obtain temporal variation of the modes, POD coefficients are evaluated by projecting each of the modes onto the disturbance flow field. To obtain a reasonable description of the flow field by reconstructing and superimposing the calculated POD modes, only a limited number of the most energetic modes are required.

Experiments of turbulent pipe flows^{17–20} have been able to capture near-wall turbulent structures albeit with difficulty due to the immensely time-consuming procedure of computing the correlation matrix. The

advent of more sophisticated flow imaging techniques such as high-resolution particle image velocimetry (PIV) enabled further progress in the analysis of coherent structures in turbulent flows. ²¹ In addition to experimental studies, there have been several DNS studies investigating the structure of turbulence for pipe as well as channel flows. The ability to extract disturbance signals from all points in the domain simplifies the process of calculating the correlation matrix. For channel flows, a direct correlation between the number of modes required to reasonably recreate the disturbance field and the Reynolds number was observed. ^{22–24}

The present study makes use of a variation of POD called snapshot POD.²⁵ In snapshot POD, it is assumed that the flow field can be separated into a spatial and a temporal component. This assumption leads to a significant reduction in the computational cost associated with the computation of POD as it leads to a reduction in the dimension of the correlation matrix. The aim of this study is to be able to identify and characterize the various coherent motions which are exhibited in the case of a rotating pipe flow. As mentioned by Marusic $et\ al.$,²⁶ the coherent structures within wall-bounded turbulent flows can be classified into four categories — (i) near-wall streaks in the viscous sub-layer, (ii) horseshoe or hairpin vortices, (iii) large scale motions (LSMs), and (iv) very large scale motions (VLSMs).

POD analyses utilizing data from several experiments as well as numerical studies has shed light on the most energetic structures which exist in turbulent pipe flows. Hellström $et\ al.^{21}$ demonstrated large-scale flow features can be reconstructed using a few of the most energetic modes obtained from POD. DNS performed at Re=24,580 by Wu $et\ al.^{27}$ showed the presence of roll-like structures in the lower order modes of the flow. This behavior was also observed in experiments by Hellström $et\ al.^{21}$ and Bailey and Smits²⁰ which supported the postulate of Kim & Adrian²⁸ that VLSMs can be created by the alignment of LSMs.

In the current study, POD is applied to the disturbance flow field for rotating turbulent pipe flows exhibiting turbulence suppression. The results obtained are then compared to those obtained from POD analysis of non-rotating turbulent pipe flows to gain understanding about the structural changes introduced by the turbulence.

This manuscript is organized as follows: Section II discusses the solver details chosen for the current DNS, computational domain considerations, and simulation requirements. A basic overview of the turbulent flow characteristics are provided in Sections A-C which provide mean velocity profiles, as well as an analyses of the effects of rotation on Reynolds stresses and turbulent kinetic energy. Section D discusses POD results for the rotating and non-rotating pipe flow.

II. Computational Methods

Simulations were conducted using the spectral element solver Nek5000, developed by Fischer et al.²⁹ Nek5000 is a higher-order accurate, open source, spectral element solver used to solve the incompressible Navier-Stokes equations and is well-known for its (spectral) accuracy, favorable dispersion properties, and efficient parallelization.³⁰ The spectral element method is based on a weighted-residual approach for spatial discretization. For parallel computations, Nek5000 utilizes the message passing interface (MPI) protocol and has shown excellent scaling characteristics on HPC systems — making it well-suited for large-scale turbulence flow computations. The mesh is comprised of hexahedral elements with the solution being composed of N^{th} -order tensor product polynomials within each element. Local lexicographical ordering within each macro element, as well as the need to evaluate only $\mathcal{O}(EN^4)$ discrete operators, which typically have $\mathcal{O}(EN^6)$ non-zeros, leads to the cache and vectorization efficiency.²⁹ A semi-implicit time-integration scheme is used where the viscous terms of the Navier-Stokes equations are treated implicitly with third-order backward differentiation (BDF3) and the nonlinear advection terms are explicitly extrapolated in time with third-order accuracy.

Nek5000 minimally uses external libraries to increase compile speed, and matrix operations are implemented in assembler code M×M routines to speed up computations. Furthermore, Nek5000 tests each of the three parallel algorithms at the beginning of each run to determine which behaves optimally — thus parallelism is automatically tuned for each machine.²⁹ The algebraic multi-grid (AMG) solver was chosen throughout this work from the different pressure Poisson solvers available in Nek5000.

The choice of the domain size such that a fully developed flow can be obtained is an important issue both for numerical simulations and experiments. Flow visualizations by Nishibori et al.⁷ showed that coherent flow structures form in the center of the pipe at high rotation rates. Thus, to avoid a negative impact of the domain size on the computational results, it has to be ensured that the fluctuating velocities measured

at two locations separated by a streamwise distance of $\mathcal{O}(L)$ are uncorrelated. Orlandi and Fatica¹¹ found that a domain size of L/D=7.5 for Re=4,900 and N=2 is sufficient to resolve the largest flow structures within the domain. Khoury $et~al.^{30}$ showed a domain size of L/D=12.5 to be sufficient for pipe flows at Reynolds numbers up to Re=37,700, being the more conservative estimate, this domain was chosen for the current simulations. As shown in Fig. 2, periodic boundary conditions were used at the inflow and outflow of the domain to allow the simulations to reach a fully developed state.

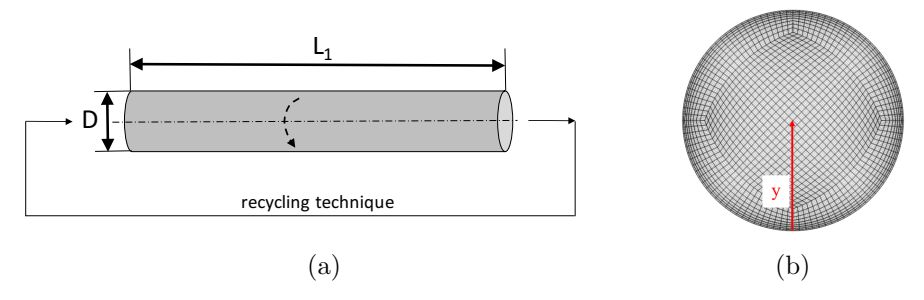


Figure 2. (a) Simulation domain and (b) mesh cross-section for the fully developed turbulent flow simulations.

The different grid size, $N_{\Delta x}$, for Re=19,000 turbulent pipe flow case is provided in Table 1. Sufficient temporal and spatial resolution is required to thoroughly study the intricate nature of turbulence and the physical mechanisms of turbulence suppression. The computational mesh shown in Fig. 2b. It was chosen to resolve the wide range of different turbulent scales. The radial, azimuthal and streamwise grid spacings are reported in y^+ -units and different ranges are provided because the mesh varies within the computational domain. Note that the friction factor (or skin friction values) used to calculate the grid spacings in y^+ -units were obtained from non-rotating turbulent pipe flow simulations. The provided grid spacings in y^+ -units are conservative estimates for the rotating pipe flow simulations because the skin friction values were expected to be lower for a rotating pipe due to the relaminarization process.

Re	f	$\Delta r^+/\Delta R\Theta^+/\Delta z^+$	$N_{\Delta x} \times 10^6$	Δt	$N_{\Delta t}$	ft	fa	
19,000	0.0270	0.15 - 4.5 / 1.5 - 4.8 / 3.0 - 10.	440	0.00053	400,000	14	6.5	

Table 1. Details of turbulent pipe flow simulations assuming a streamwise extent of 15D, where Re refers to the Reynolds number, $f = 8u_{\tau}^2/U_b^2$ is the friction factor, $N_{\Delta x}$ is the number of grid points in the computational domain, Δt is the chosen timestep, $N_{\Delta t}$ is the number of total timesteps, and Δr^+ , $\Delta R\Theta^+$ and Δz^+ are the grid spacings measured in y^+ -units. Note that for the grid spacings different ranges are provided because the mesh is non-uniform. The flow through time is ft, and, finally, fa is the number of flow throughs over which temporal averaging was conducted.

Since the convective terms of the incompressible Navier-Stokes equations are treated with an explicit time-integration scheme, to allow for a stable numerical solution the non-dimensional timestep, Δt , corresponds to a CFL number of less than 1. The timesteps provided in Table 1 were chosen to ensure CFL=0.75. To obtain fully-converged turbulent statistics we require a total compute time of at least ten flow through times which includes an initial transient. The total number of timesteps, $N_{\Delta t}$, reported in Table 1 are based on flow through times providing sufficient accuracy in the turbulent statistics that can be obtained from the simulations, where the number of flow throughs during which averaging occurred is given by fa in Table 1.

III. Results

To provide an overview of rotational effects on turbulent pipe flows some of our previous results are included in this manuscript, such as plots of mean profiles, Reynolds stresses, and turbulent kinetic energy for different Reynolds and rotation numbers. To obtain turbulent statistics the instantaneous flow data was temporally averaged at each point in the computational domain at run-time and spatially averaged in the periodic directions, *i.e.*, streamwise and azimuthal directions. Values were directly averaged in the streamwise direction, as the size of spectral elements are uniform in this direction, but interpolation onto a radially uniform grid was required for azimuthal averaging. In the following discussion, direct and derived flow quantities enclosed by < * > have been spatially and temporally averaged.

Our prior works have focused on quantifying turbulence suppression for rotating flows and coming up

with a rigorous metric for measuring the degree of turbulence suppression in the flow instead of simply providing a mainly qualitative description of the phenomena.

In prior works turbulence suppression was mainly quantified by considering the changes in the mean flow profiles manifesting in a reduction in skin friction and pressure loss. However, the skin friction coefficient is completely determined by the state of the flow at the wall and while mixing towards the wall is inhibited it was shown in our previous study that an important feature of the rotating turbulent pipe flow is that turbulence is redistributed throughout the cross-section of the pipe. It turns out that turbulence suppression is not clearly detectable when simply considering the mean flow quantities. Furthermore, it appears that the turbulent flow inside a rotating pipe is comprised of two competing flow regimes *i.e.*, the pipe flow regime and the flow inside a rotating cylinder regime. These two regimes were introduced following the rationale that rotation destabilizes a laminar pipe flow and turbulence introduced into rotating cylinder flow experiences suppression. The upcoming sections provide an overview of the mean flow characteristics in terms of mean flow profiles in Section A and mean turbulent flow characteristics by considering radial profiles of turbulent kinetic energy and the individual Reynolds stress components in sections B and C, respectively.

A. Mean Velocity Profiles

Mean streamwise velocity profiles normalized by the bulk velocity are presented in Fig. 3 for different Reynolds numbers Re=5,300,11,700, and 19,000 and rotation numbers ranging from N=0 to N=3. The mean velocity profiles in Fig. 3a display a strong dependence on the rotation number but small dependence on the Reynolds number. Kikuyama $et\ al.^6$ conducted experiments to study the effects of rotation on turbulent pipe flows and made similar observation. The reduction in mean streamwise velocity towards the wall (in the region 0.1 < y < 0.4) was explained by reduced turbulent mixing towards the wall which then leads to high velocity flow concentrated towards the center of the pipe. The overall change in the shape of the velocity profiles from a full turbulent profile tending towards a laminar parabolic velocity profile when adding rotation to the turbulent pipe flow was previously used as an indicator of turbulence suppression.

The velocity profiles in inner-scale are shown in Fig. 3b where the mean streamwise velocity was normalized with the friction velocity u_{τ} . In the viscous sub-layer all profiles collapse to the inner solution (as was expected) but in the log-layer a strong deviation from the log-law can be observed. With increasing rotation numbers the deviation away from the turbulent pipe flow profile becomes apparent closer to the wall (in the region 0.1 < y < 0.4).

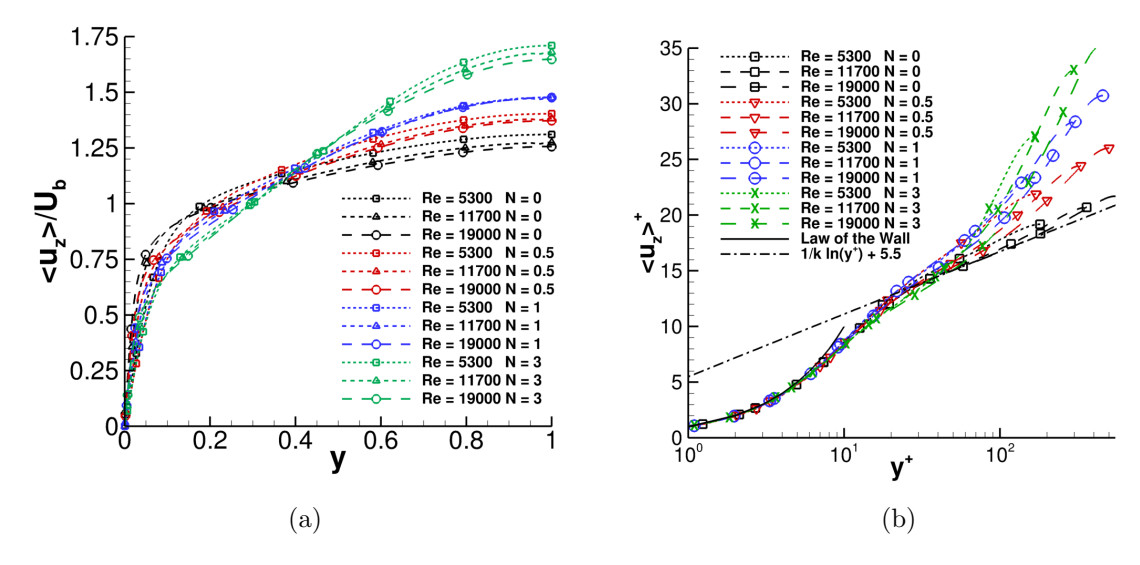


Figure 3. Mean streamwise velocity profiles for all Reynolds numbers (a) normalized with bulk velocity U_b and (b) in inner scaling.

As for the mean streamwise velocity profiles similar observation can be made for the mean azimuthal velocity profiles displayed in Fig. 4a for Re=19,000. The mean azimuthal velocity is normalized with the velocity at the wall, U_w , in an inertial (laboratory) reference frame. In addition, Fig. 4b provides swirl profiles which were computed for an observer in a reference frame rotating with the pipe. It can be observed

that the magnitude in the peak of the swirl profiles show a dependence on the rotation number, N, while the location of the peak appears to be nearly insensitive to N. The swirl profiles display a much stronger dependence on the Reynolds number than the streamwise velocity profiles with a reduction in the peak and shift towards the center for lower Reynolds numbers.

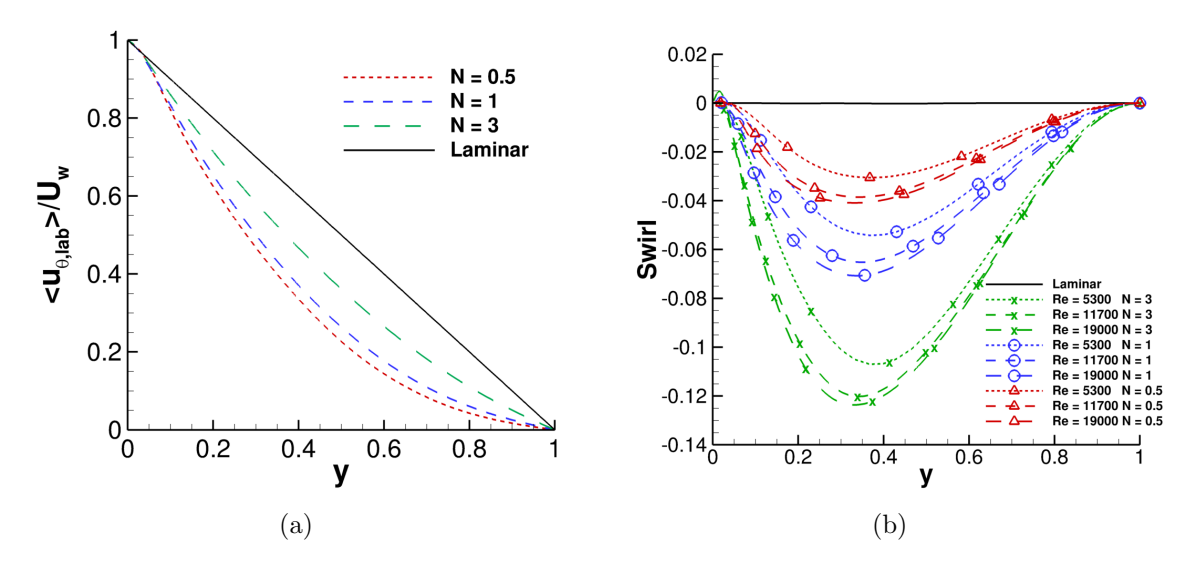


Figure 4. (a) Mean azimuthal velocity (non-rotating reference frame) profiles normalized by the velocity of the wall for Re = 19,000 and (b) a comparison of swirl profiles.

A comparison of the friction Reynolds number defined as $Re_{\tau} = u_{\tau}D/\nu$ in Fig. 5a displays a trend which is attributed to the reduction of the near wall gradient in the velocity profile. While large reductions in the friction Reynolds number can be observed for lower rotation numbers N the reduction appears to level off when approaching the largest rotation number of N=3. This result appears to indicate a reduction in the efficiency of reducing near-wall velocity gradients with increasing rotation numbers. In order to more clearly visualize the reduction the friction Reynolds number the data was normalized with the values obtained for the non-rotating turbulent pipe flow. A reduction in friction Reynolds number of more than 15% can be observed up to N=1 for the two larger Reynolds number cases while an insignificant reduction occurs when increasing the Rotation number further beyond N=1 (here, up to N=3 only).

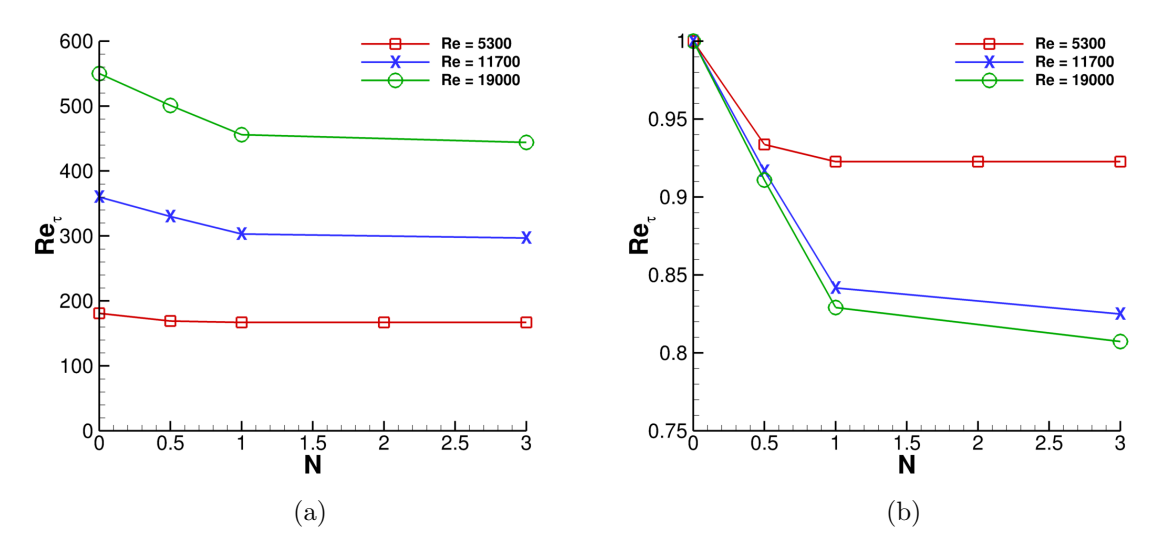


Figure 5. (a) Comparison of friction Reynolds number for different rotation Numbers. (b) Relative reduction of friction Reynolds number (normalized by non-rotating friction Reynolds number).

B. Turbulent Kinetic Energy

Although the previous section showed some general trends of the mean flow features when adding rotation to a turbulent pipe flow turbulent kinetic energy appears to be the most sensible candidate for quantifying turbulence suppression. The turbulent kinetic energy profiles capture the effects on turbulence throughout the entire cross-section of the pipe, including the redistribution of turbulent kinetic energy.

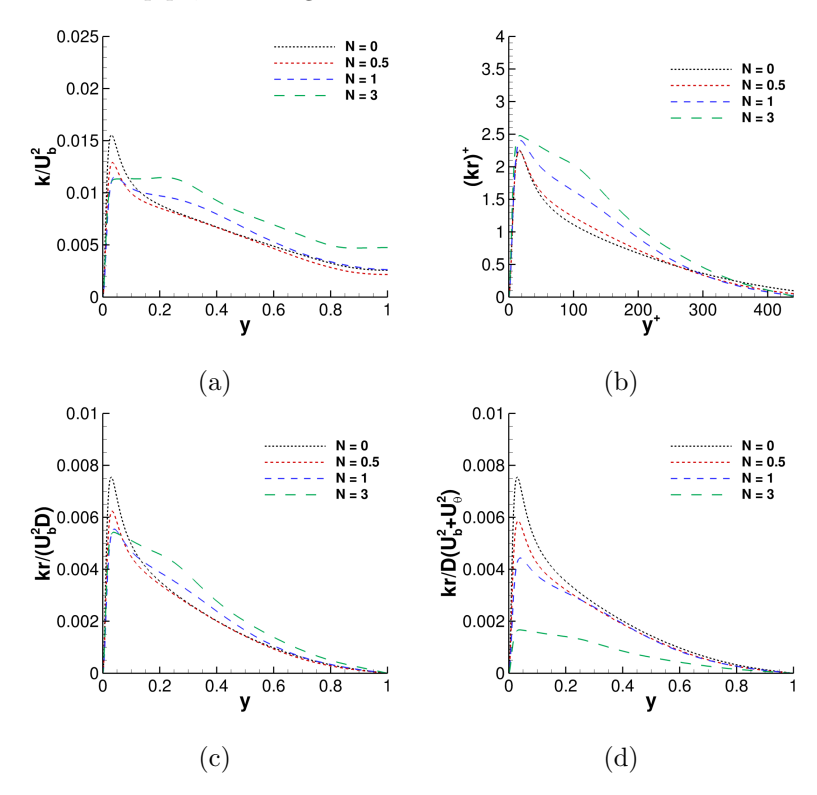


Figure 6. (a) Turbulent kinetic energy normalized by bulk velocity squared, Turbulent kinetic energy multiplied by radial position and normalized by pipe diameter D as well as (b) friction velocity squared, u_{τ}^2 , (c) bulk velocity squared, U_b^2 , and (d) total mean kinetic energy for $Re=19{,}000$.

Fig. 6a shows turbulent kinetic energy profiles normalized by the bulk velocity squared. This plot does not show a clear reduction of turbulent kinetic energy (or turbulence suppression). Inner-scaled turbulent kinetic energy profiles multiplied by the local radius to account for the area-weighted contribution in the cylindrical coordinate system are shown in Fig. 6b. Near the wall, the turbulent kinetic energy profiles appear to collapse and the near-wall peak is nearly unaffected by the rotation number. The key observation is, however, that this plot suggests an increase in turbulent kinetic energy throughout the pipe's cross-section which is contrary to the presumption of turbulence suppression for the rotating turbulent pipe flow. Further, the plots indicate an increase of turbulent kinetic energy between the wall and the center of the cross-section. Fig. 6c shows turbulent kinetic energy in outer scaling again compensating for the area with the radius and normalizing with the bulk velocity. In outer-scale, a reduction in the inner peak of turbulent kinetic energy can be observed. Nevertheless, towards the center an increase in turbulent kinetic energy can still be observed. The trends for the lower Reynolds number cases (not shown here) display less reduction in the near-wall peak and a larger increase in turbulent kinetic energy towards the center. In outer-scale, only a slight reduction in turbulent kinetic energy can be observed and mainly for lower rotation numbers (see also Fig. 7a).

With increasing rotation number, an increasing contribution of the mean azimuthal velocity component towards the mean total kinetic energy is present. Therefore, it appears more sensible to normalize the turbulent kinetic energy by the mean total kinetic energy including the contribution from the azimuthal velocity component. A clear suppression of turbulent kinetic energy throughout the entire cross-section for sufficiently large Reynolds numbers can be observed with this normalization in Fig. 6d.

Figs. 7a and 7b essentially summarize the previous results. The plots display the change in the total

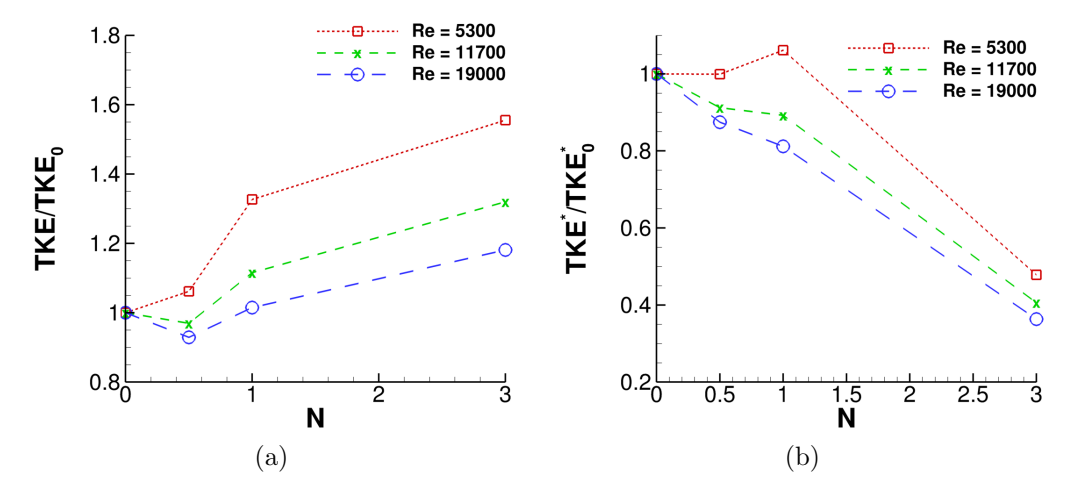


Figure 7. Ratio of total turbulent kinetic energy normalized by mean kinetic energy to that of the non-rotating case considering (a) only the streamwise velocity component and (b) the total mean kinetic energy.

turbulent kinetic energy considering the normalization purely based on the streamwise velocity component and when also adding the contribution from the azimuthal velocity component. Finally, it can be concluded that turbulence suppression can only be observed when considering the total mean kinetic energy and only at sufficiently large Reynolds numbers. This is in contrast to prior works that mainly considered the skin friction or pressure drop as an indicator for turbulence suppression where a clear trend of skin friction reduction has been observed for all Reynolds numbers and rotation numbers.

C. Reynolds Stresses

As has been discussed in the previous sections for the rotating turbulent pipe flow there are competing mechanisms at play non-uniformly affecting the turbulent flow throughout the cross-section. When considering turbulent kinetic energy the effects of rotation are projected onto a single scalar quantity. However, rotation does not only affect the magnitude of the turbulent fluctuations but also the orientation. Next, the different components of the Reynolds stress tensor are considered and their variations throughout the pipe's cross section providing an improved understanding of the orientation of the turbulent fluctuations. For this purpose, the Reynolds stress tensor was transformed into its principal axes by computing the eigenvalues and eigenvectors. The transformation results into a diagonal matrix eliminating the shear terms. Fig. 9a displays the principal stresses throughout the pipe's cross section. The largest eigenvalue is denoted by σ_1 , the second largest eigenvalue is denoted by σ_2 and σ_3 refers to the smallest eigenvalue. Note that in the non-rotating case the eigenvectors associated with the two largest eigenvalues are lying in the (z, r)-plane and the eigenvector associated with the smallest eigenvalue points in the θ direction. The 1st principle Reynolds stress shows a clear reduction in the peak when the rotation number is increased. However, similar to turbulent kinetic energy σ_1 shows an increase towards the middle of the cross section of the pipe. The second largest eigenvalue does not provide a clear trend with a minor reduction in the peak for smaller rotation numbers and an increase of σ_2 throughout the cross section for large rotation numbers. This observation is consistent with what has been shown for other turbulent flow quantities which can be attributed to a change in the turbulent flow characteristics when the rotation number exceeds N=1.

The orientation of the eigenvectors is tracked by computing the angle between the principle axes and the axes of the cylindrical coordinate system as illustrated in Fig. 8. Fig. 9b displays the angles ϕ_{rz} in the r-z plane for the 1^{st} and 3^{rd} principle axes. An understanding of the change in the orientation of the principle axes can be gained by comparing the eigenvector directions for the rotating pipe flow against the case with no rotation. For the non-rotating pipe flow, the 1^{st} principle axis is aligned with the streamwise direction at the wall y=0 and in the center of the pipe at y=1. Away from the wall and the center of pipe, the 1^{st} principle axis points slightly upwards and is oriented at approximately 20° to center axis. The third principle axis which is naturally orthogonal to the 1^{st} principle axis follows a similar trend whereby it is aligned with the radial direction at the wall and in the center of the pipe. When adding rotation to the turbulent pipe flow the 1^{st} principle axis is more closely aligned with the axis of rotation, thus, a reduction of ϕ_{rz} can be

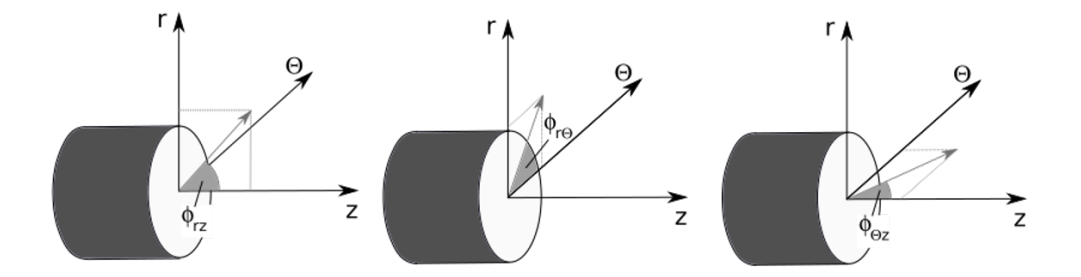


Figure 8. Representation of the angles between the principle axes and the cylindrical coordinate system.

observed in the middle section (y >> 0 and y << 1) of the pipe. When tracking the adjustment of the 2^{nd} and 3^{rd} principle axes in the $r-\theta$ plane a similar observation can be made. While for the non-rotating turbulent pipe flow the 2^{nd} principle axis is aligned with the azimuthal direction throughout the cross section of the pipe adding rotation causes the 2^{nd} principle axis to point away from the azimuthal direction. The misalignment away from the azimuthal direction becomes larger with increasing rotation number.

The formation of helical structures near the wall which have been reported by Orlandi & Faticia¹¹ for the rotating pipe flow may be the cause of the change in the orientation of the principle axes. By employing coherence analysis, here POD in particular, the extent and magnitude of the turbulent structures can be better understood, allowing for a greater understanding of both the spatial extent of these structures as well as the influence these structures exhibit on the flow field.

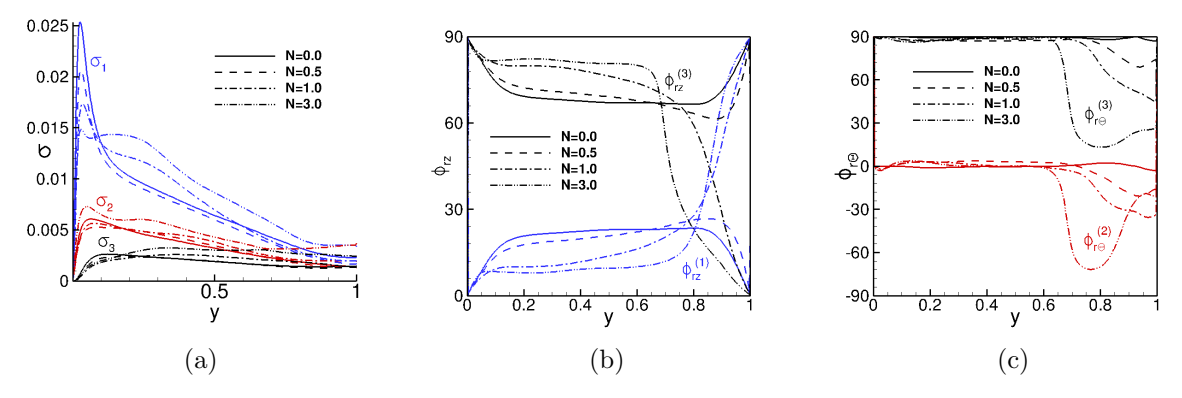


Figure 9. (a) Principle Reynolds stresses and eigenvector angles in (b) the r-z plane and (c) the $r-\theta$ plane for Re=19,000.

D. Proper Orthogonal Decomposition

To extract coherent flow structures from the turbulent flow field a special variant of the classical POD method is employed, namely the method of snapshots, which utilizes a collection of instantaneous snapshots of the flow field. Commonly, snapshot POD is employed if the size of the data N is significantly larger than the number time instances M. The eigenvalue problem based on the temporal correlation matrix is much smaller in the case of M << N than the eigenvalue problem obtained in classical POD but it provides the same dominant spatial modes. Thus, snapshot POD allows a decomposition of the turbulent flow field into a set of orthonormal basis functions whereby the modes are ordered by their energy content. In this work, the snapshot POD modes are computed following Ref. 32. POD was conducted using 800 snapshots at equidistant time intervals of $5.25 \times 10^{-2} (100\Delta t)$ corresponding to a total bulk displacement of 3.36L (21D). As the turbulent pipe flow displays a geometric symmetry around the center axis the POD modes in the azimuthal direction are reduced to a Fourier series. Since these modes are known a priori we apply a Fourier decomposition in azimuthal direction which allows to accelerate the convergence of the POD modes. Spatial discrete Fourier transforms were conducted at 100 radial locations on 150 discrete cross-sections within the domain.

In the current work, it is assumed that the velocity vector, $\mathbf{v}(\mathbf{x},t) = (v_1, v_2, v_3)^T = (u'_r, u'_\theta, u'_z)^T$, is defined over a region of interest Ω . The predefined energy norm can then be defined as a weighted sum (here, $w_k = 1$) of the velocity vector components

$$|\mathbf{v}|_{\Omega}^{2} = \int_{\Omega} \left(\sum_{k=1}^{3} w_{k} v_{k}^{2} \right) d\mathbf{x}. \tag{1}$$

POD seeks a modal decomposition of the flow field into POD modes which optimally converge the above energy norm defined in Eq. 1.

The m-th POD mode, $\Psi^{(m)}$, can be computed as

$$\mathbf{\Psi}^{(m)}(\mathbf{x}) = \sum_{n=0}^{N} r_n^{(m)} \mathbf{v}(\mathbf{x}, t_n), \tag{2}$$

where n sums over the N timesteps (n = 0 to N), $\mathbf{v}(\mathbf{x}, t_n)$ is the snapshot of the velocity field at time instant t_n , and $r_n^{(m)}$ are the components of the m-th right eigenvector. The eigenvector $\mathbf{r}^{(m)}$ and the eigenvalue $\lambda^{(m)}$ are the solution to the eigenvalue problem defined as

$$\underline{\mathbf{C}}\mathbf{r}^{(m)} = \lambda^{(m)}\mathbf{r}^{(m)}.\tag{3}$$

The (i,j)-th component of temporal correlation tensor $\underline{\mathbf{C}}$ is given as

$$C_{i,j} = \frac{1}{N} \left[\mathbf{v}(\mathbf{x}, t_i), \mathbf{v}(\mathbf{x}, t_j) \right], \tag{4}$$

where $[\mathbf{v}(\mathbf{x}, t_i), \mathbf{v}(\mathbf{x}, t_j)]$ refers to the inner product defined over the domain Ω . Finally, the time-coefficients can be computed as

$$a^{(m)}(t) = \frac{1}{\lambda^{(m)}} \left[\mathbf{v}(\mathbf{x}, t), \mathbf{\Psi}^{(m)}(\mathbf{x}) \right], \tag{5}$$

and the flow field can be reconstructed using the time-coefficients and spatial POD modes

$$\mathbf{v}(\mathbf{x},t) \approx \sum_{m=0}^{M} a^{(m)}(t) \mathbf{\Psi}^{(\mathbf{m})}(\mathbf{x}). \tag{6}$$

Sorting each mode by energy content allows for the identification of the most significant modes. As POD decomposition is purely based on optimization principles with respect to a predefined energy norm the results need to be interpreted carefully. Finally, it should be noted that there are important differences between classical POD and snapshot POD. Most importantly for the current work, mixing of modes may occur in snapshot POD which can result in a non-optimal set of modes with energy being not properly distributed.³³

POD analysis has been conducted for the non-rotating (N=0) and rotating (N=1) turbulent pipe flow cases. The POD analysis results for the non-rotating turbulent pipe flow are in good agreement with the results previously presented in Hellström and Smits. 34 Fig. 10a and 10b shows the relative energy content for the first five POD modes for the non-rotating N=0 and rotating N=1 turbulent pipe flows. For the nonrotating case, it can be seen that the highest energy modes contain approximately 4-5% of the total energy which is consistent with results in Hellström and Smits.³⁴ The inclusion of rotation in the flow, however, causes a significant increase in energy contained within the lowest POD modes, as shown in Fig. 10b, where the highest energy mode contains approximately 15\% of the total energy. Further, the two highest energy mode contain jointly more than 20% of the total energy. The increase in energy within the lowest modes of the flow may also explain the formation of a second peak in turbulent kinetic energy shown in Fig. 6a, as this peak coincides with the location of the maximum amplitude of the lowest modes. Approximately 30% of the total energy in the non-rotating flow is represented by integrating over the first radial mode and first 20 azimuthal modes, while extending this integration over the first five radial modes represents approximately 57% of the total energy of the non-rotating case. When this integration is conducted for the rotating case, the corresponding values are 33% and 62%, respectively, indicating that the rotating turbulent pipe flow is dominated by small number of highly energetic modes.

The streamwise component of the first radial mode for each flow is shown in Fig. 11. Each mode has been normalized by its l2-norm, and azimuthal modes 5, 10, 15, 20, 25, 35, 40, 45, and 50 are shown.

The wall normal extent of the modes decreases with decreasing azimuthal length scale in each case. The inclusion of rotation does not significantly affect the mode shapes of the streamwise component of the first radial mode, though it should be noted that convergence has not yet been fully reached for the rotating case. However, these results indicate that the structure of the streamwise component of these modes is not significantly impacted by rotation, while the energy content within each mode, especially the lowest modes, is dramatically altered by the addition of rotation to the flow.

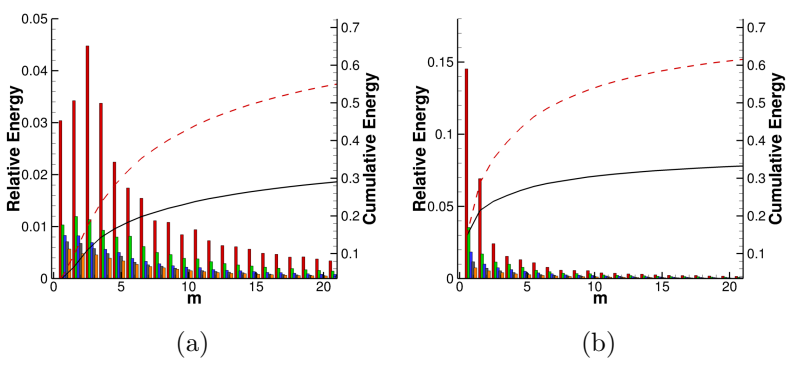


Figure 10. Relative energy of the first five POD modes for (a) N = 0 and (b) N = 1. The red line indicates the cumulative energy contribution from each mode and black indicates the cumulative energy contribution from the first mode only.

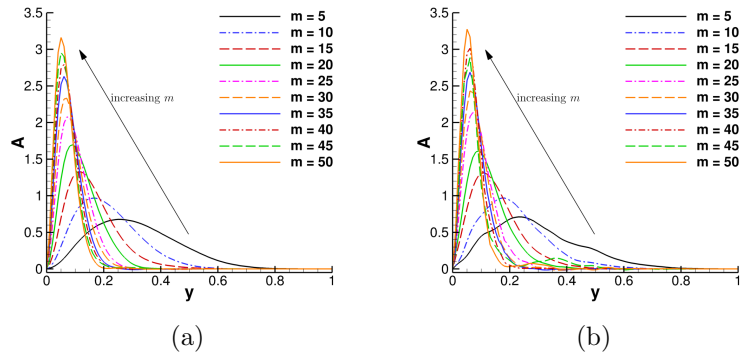


Figure 11. Streamwise component of the first radial mode and azimuthal modes m = 5, 10, 15, 20, 25, 30, 35, 40, 45, and 50 for (a) N = 0 and (b) N = 1. Note that the analysis of the rotational case is still ongoing, and these mode shapes represent preliminary results.

Cross-sectional visualizations of the reconstructed azimuthal modes (m=5 and m=10) for the first radial mode for the N=0 case based on the radial mode shapes in Fig. 11a are shown in Figure 12. Similarly, Fig. 13 displays the same subset of azimuthal modes for the first radial mode for the N=1 case based on the radial mode shapes in Fig. 10b. A direct comparison of the three velocity components for the different azimuthal modes in Figs. 12 and 13 highlights some changes in structure of the flow when rotation is introduced. These changes are more prominent in the radial and azimuthal directions. The structures in the streamwise velocity component for N=1 (Fig. 13) have moved closer to the wall when compared to that for N=0 (Fig. 12). On the contrary, the peaks for the radial components move away from the wall for the rotating turbulent pipe flow. Additionally, a decrease is evident for the wall normal extent of the azimuthal velocity component of each mode for rotating case.

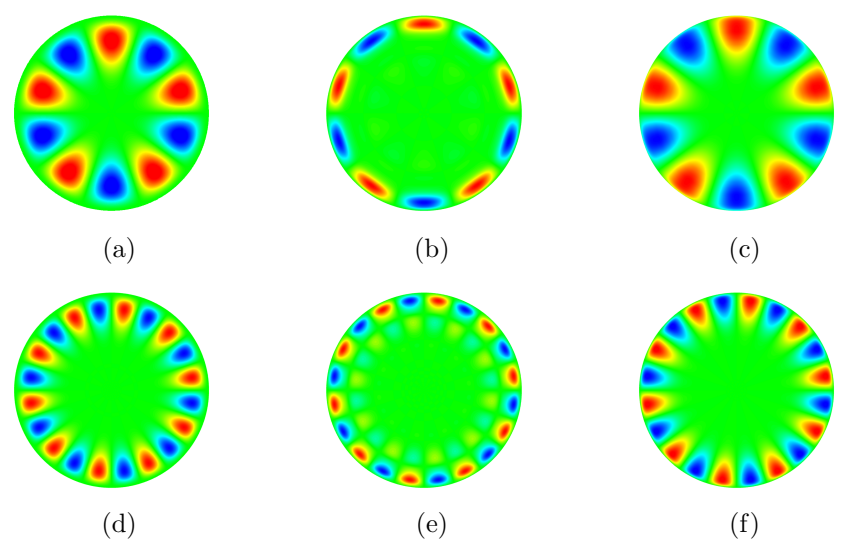


Figure 12. Visualization of the first radial mode and fifth azimuthal mode for the (a) streamwise, (b) radial, and (c) azimuthal velocity components for N=0. Visualization of the first radial mode and tenth azimuthal mode for the (d) streamwise, (e) radial, and (f) azimuthal velocity components for N=0.

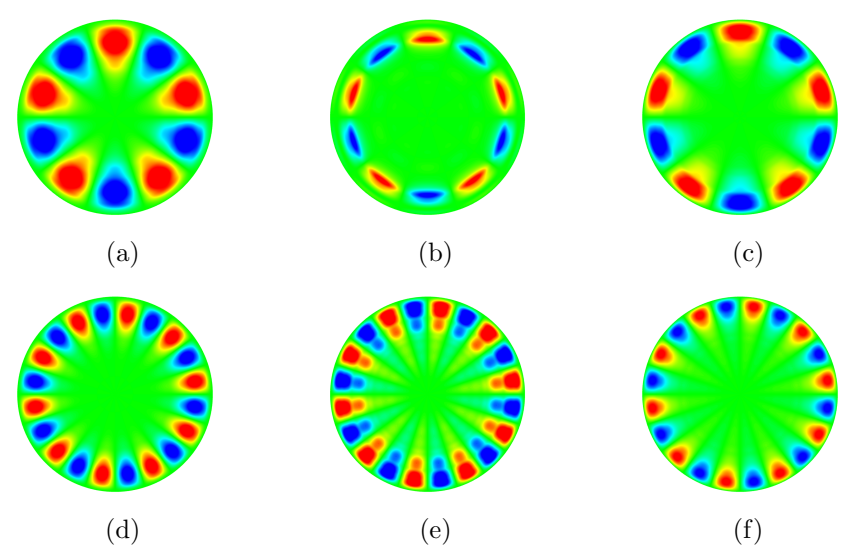


Figure 13. Visualization of the first radial mode and fifth azimuthal mode for the (a) streamwise, (b) radial, and (c) azimuthal velocity components for N=1. Visualization of the first radial mode and tenth azimuthal mode for the (d) streamwise, (e) radial, and (f) azimuthal velocity components for N=1.

IV. Conclusions

This paper presented simulation results from highly-resolved DNS of rotating pipe flow for Reynolds numbers Re = 5,300, 11,700, and 19,000 at rotation rates up to N = 3. The DNS data showed a strong influence of rotation on the turbulent flow field. The change in the turbulent flow characteristics were quantified by computing profiles of the mean velocities, the turbulent kinetic energy, and the principal values and directions of the Reynolds stress tensor. The mean streamwise velocity component showed a reduction in the near-wall gradient leading to a reduction in skin friction and pressure drop. Further, a reduction of turbulent kinetic energy was observed throughout the cross-section of the pipe when normalizing the turbulent kinetic energy by the total mean kinetic energy considering both the mean streamwise and azimuthal velocity components. Moreover, a redistribution and reorientation of the Reynolds stress tensor was observed when adding rotation to the turbulent pipe flow. These results indicate a significant change in the topology of the flow for large rotation numbers and as such in the organization, e.g. coherence, of the flow. Finally, proper orthogonal decomposition was conducted to gain insight into the effects of rotation

on the flow structures within rotating turbulent pipe flow. A significant increase in the coherence of the turbulent pipe flow was noted in the presence of rotation. In future work, the classical POD approach will be used to avoid possible mode mixing leading to non-optimal mode sets and an improper energy distribution that may occur for snapshot POD.

Acknowledgments

This work was supported by funding from the National Science Foundation under award CBET-1706346 with Dr. R. Joslin as Program Manager.

This research is part of the Blue Waters sustained-petascale computing project, which is supported by the National Science Foundation (awards OCI-0725070 and ACI-1238993) and the state of Illinois. Blue Waters is a joint effort of the University of Illinois at Urbana-Champaign and its National Center for Supercomputing Applications.

This work used the Extreme Science and Engineering Discovery Environment (XSEDE), which is supported by National Science Foundation grant number ACI-1548562.³⁵ Research was conducted using the Stampede2 and Comet HPC systems through allocation TG-CTS180008.

References

¹Davis, J., Ganju, S., and Brehm, C., "Direct Numerical Simulations of Turbulence Suppression in Rotating Pipe Flows," Parallel CFD Conference Proceeding, May 14-18, Indianapolis, Indiana, 2018.

²Davis, J., Ganju, S., and Brehm, C., "Direct Numerical Simulations of Rotating Turbulent Pipe Flows at Moderate Reynolds Numbers," APS DFD, 18-20 November, Atlanta, 2018.

³Davis, J., Ganju, S., Bailey, S., and Brehm, C., "A DNS Study to Investigate Turbulence Suppression in Rotating Pipe Flows," AIAA Aviation and Aeronautics Forum and Exposition Dallas, TX, June 17 to June 21,, 2019, AIAA Paper 2019.

⁴Borchetta, C., Brehm, C., and Bailey, S., "On the Development of an Apparatus to Examine Rotating Pipe Flow at High Rotation Numbers," APS DFD, 18-20 November, Atlanta, 2018.

⁵Murakami, M. and Kikuyama, K., "Turbulent flow in axially rotating pipes," *Journal of Fluids Engineering*, Vol. 102, No. 1, 1980, pp. 97–103.

⁶Kkikuyama, K., Murakami, M., Nishibori, K., and Maeda, K., "Flow in an Axially Rotating Pipe: A calculation of flow in the saturated region," *Bull. JSME*, Vol. 26, No. 214, 1983, pp. 506–513.

⁷Nishibori, K., Kikuyama, K., and Murakami, M., "Laminarization of turbulent flow in the inlet region of an axially rotating pipe." *JSME International Journal*, Vol. 30, No. 260, 1987, pp. 255–262.

⁸Reich, G. and Beer, H., "Fluid flow and heat transfer in an axially rotating pipe I. Effect of rotation on turbulent pipe flow," *International Journal of Heat and Mass Transfer*, Vol. 32, No. 3, 1989, pp. 551–562.

⁹Feiz, A., Ould-Rouis, M., and Lauriat, G., "Turbulence statistics in a fully developed rotating pipe flow," *Journal of Enhanced Heat Transfer*, Vol. 12, No. 3, 2005.

¹⁰White, A., "Flow of a fluid in an axially rotating pipe," *Journal of Mechanical Engineering Science*, Vol. 6, No. 1, 1964, pp. 47–52.

¹¹Orlandi, P. and Fatica, M., "Direct simulations of turbulent flow in a pipe rotating about its axis," *Journal of Fluid Mechanics*, Vol. 343, 1997, pp. 43–72.

¹²Orlandi, P. and Ebstein, D., "Turbulent budgets in rotating pipes by DNS," International Journal of Heat and Fluid Flow, Vol. 21, No. 5, 2000, pp. 499–505.

¹³Orlandi, P. and Fatica, M., "Direct simulations of turbulent flow in a pipe rotating about its axis," *Oceanographic Literature Review*, Vol. 7, No. 45, 1998, pp. 1257.

¹⁴Bradshaw, P., "The analogy between streamline curvature and buoyancy in turbulent shear flow," *Journal of Fluid Mechanics*, Vol. 36, No. 1, 1969, pp. 177–191.

¹⁵Brehm, C., Davis, J., Ganju, S., and Bailey, S., "A Numerical Investigation of the Effects of Rotation on Turbulent Pipe Flows," TSFP11 30 July - 2 August, Southampton, UK, 2019.

¹⁶ Ashton, N., Davis, J., and Brehm, C., "Assessment of the Elliptic Blending Reynolds Stress Model for a Rotating Turbulent Pipe Flow Using New DNS Data," AIAA Aviation and Aeronautics Forum and Exposition Dallas, TX, June 17 to June 21,, 2019, AIAA Paper 2019.

¹⁷Aubry, N., Holmes, P., Lumley, J. L., and Stone, E., "The dynamics of coherent structures in the wall region of a turbulent boundary layer," *Journal of Fluid Mechanics*, Vol. 192, 1988, pp. 115–173.

¹⁸Bakewell, H. P. and Lumley, J. L., "Viscous Sublayer and Adjacent Wall Region in Turbulent Pipe Flow," The Physics of Fluids, Vol. 10, No. 9, 1967, pp. 1880–1889.

¹⁹Herzog, S. and Lumley, J. L., "Determination of Large Eddy Structures in the Viscous Sublayer: A progress report," *Proceedings of the Dynamic Flow Conference 1978 on Dynamic Measurements in Unsteady Flows*, edited by B. W. Hansen, Springer Netherlands, Dordrecht, 1978, pp. 869–885.

²⁰Bailey, S. C. C. and Smits, A. J., "Experimental investigation of the structure of large- and very-large-scale motions in turbulent pipe flow," *Journal of Fluid Mechanics*, Vol. 651, 2010, pp. 339–356.

- ²¹Hellström, L. H., Ganapathisubramani, B., and Smits, A. J., "The evolution of large-scale motions in turbulent pipe flow," *Journal of Fluid Mechanics*, Vol. 779, 2015, pp. 701–715.
- ²²Sirovich, L., Ball, K. S., and Keefe, L. R., "Plane waves and structures in turbulent channel flow," *Physics of Fluids A: Fluid Dynamics*, Vol. 2, No. 12, 1990, pp. 2217–2226.
- ²³Moin, P. and Moser, R. D., "Characteristic-eddy decomposition of turbulence in a channel," *Journal of Fluid Mechanics*, Vol. 200, 1989, pp. 471–509.
- ²⁴Ball, K. S., Sirovich, L., and Keefe, L. R., "Dynamical eigenfunction decomposition of turbulent channel flow," *International Journal for Numerical Methods in Fluids*, Vol. 12, No. 6, 1991, pp. 585–604.
- ²⁵Duggleby, A. and Paul, M. R., "Computing the Karhunen–Loéve dimension of an extensively chaotic flow field given a finite amount of data," Computers & Fluids, Vol. 39, No. 9, 2010, pp. 1704–1710.
- ²⁶Marusic, I., McKeon, B. J., Monkewitz, P. A., Nagib, H. M., Smits, A. J., and Sreenivasan, K. R., "Wall-bounded turbulent flows at high Reynolds numbers: Recent advances and key issues," *Physics of Fluids*, Vol. 22, No. 6, 2010, pp. 065103.
- ²⁷Wu, X., Baltzer, J., and Adrian, R., "Direct numerical simulation of a 30R long turbulent pipe flow at R+= 685: large-and very large-scale motions," *Journal of Fluid Mechanics*, Vol. 698, 2012, pp. 235–281.
- ²⁸Kim, K. C. and Adrian, R. J., "Very large-scale motion in the outer layer," *Phys. Fluids*, Vol. 11, No. 2, 1999, pp. 417–422.
 ²⁹Fischer, P. F., "An Overlapping Schwarz Method for Spectral Element Solution of the Incompressible Navier-Stokes Equations," *Journal of Computational Physics*, Vol. 133, 1997, pp. 84–101.
- ³⁰El Khoury, G. K., Schlatter, P., Noorani, A., Fischer, P. F., Brethouwer, G., and Johansson, A. V., "Direct numerical simulation of turbulent pipe flow at moderately high Reynolds numbers," *Flow, turbulence and combustion*, Vol. 91, No. 3, 2013, pp. 475–495.
- ³¹Sirovich, L., "Turbulence and the Dynamics of Coherent Structures," Quarterly of Applied Mathematics, Vol. XLV(3), 1987, pp. 561–590.
- ³²Brehm, C., Housman, J., and Kiris, C., "Noise Generation Mechanisms for a Supersonic Jet Impinging on an Inclined Plate," *Journal of Fluid Mechanics*, Vol. 797, 2016, pp. 809–850.
- $^{33}\mathrm{Hellstr\"{o}m},$ L. H. and Smits, A. J., "The energetic motions in turbulent pipe flow," *Physics of Fluids*, Vol. 26, No. 12, 2014, pp. 125102.
- ³⁴Hellström, L. H. and Smits, A. J., "Structure identification in pipe flow using proper orthogonal decomposition," Philosophical Transactions of the Royal Society A: Mathematical, Physical and Engineering Sciences, Vol. 375, No. 2089, 2017, pp. 20160086.
- ³⁵Towns, J., Cockerill, T., Dahan, M., Foster, I., Gaither, K., Grimshaw, A., Hazlewood, V., Lathrop, S., Lifka, D., Peterson, G. D., Roskies, R., Scott, J., and Wilkins-Diehr, N., "XSEDE: Accelerating Scientific Discovery," *Computing in Science & Engineering*, Vol. 16, No. 05, sep 2014, pp. 62–74.